OATAO
Open Archive Toulouse Archive Ouverte

Open Archive Toulouse Archive Ouverte (OATAO)

OATAO is an open access repository that collects the work of Toulouse researchers and makes it freely available over the web where possible

This is an author's version published in: http://oatao.univ-toulouse.fr/25120

Official URL: https://doi.org/10.1016/j.apsusc.2017.05.095

To cite this version:

Wang, Mengying and Thimont, Yohann and Presmanes, Lionel and Diao, Xungang and Barnabé, Antoine *The effect of the oxygen ratio control of DC reactive magnetron sputtering on as-deposited non stoichiometric NiO thin films.* (2017) Applied Surface Science, 419. 795-801. ISSN 0169-4332

Any correspondence concerning this service should be sent to the repository administrator: tech-oatao@listes-diff.inp-toulouse.fr

The effect of the oxygen ratio control of DC reactive magnetron sputtering on as-deposited non stoichiometric NiO thin films

Mengying Wang [a], Yohann Thimont [b], Lionel Presmanes [b], Xungang Diao [a], Antoine Barnabé [b,*]

[a] School of Physics and Nuclear Energy Engineering, Beihang University, Beijing, 100191, China
[b] CIRIMAT, Université de Toulouse, CNRS, INPT, UPS, Université Toulouse 3 Paul Sabatier, 118 route de Narbonne 31062, Toulouse Cedex 9, France

ARTICLE INFO

Keywords:
Nickel oxide thin films
Electrochromic device
Non-stoichiometric $Ni_{1-x}O$
Reactive DC magnetron sputtering

ABSTRACT

Non-stoichiometric $Ni_{1-x}O$ thin films were prepared on glass substrate by direct current reactive magnetron sputtering in a large range of oxygen partial pressure ($0 \leq p_{O2} \leq 1$ Pa). The dependence of the deposited film structure and properties on oxygen stoichiometry were systematically analyzed by X-ray diffraction, X-ray reflectivity, X-ray photoemission spectroscopy, Raman spectroscopy, atomic force microscopy, UV–vis measurements and electrical transport properties measurements. The deposition rates, surface morphology and opto-electrical properties are very sensitive to the oxygen partial pressure lower than 0.05 Pa due to the presence of metallic nickel cluster phase determined by X-ray diffraction, X-ray reflectivity and XPS spectroscopy. Presence of nanocrystallized NiO phase was highlighted even for $p_{O2} = 0$ Pa. For $p_{O2} > 0.05$ Pa, only the NiO phase was detected. Progressive appearance of Ni^{3+} species is characterized by a fine increase of the lattice parameter and (111) preferred orientation determined by grazing angle X-ray diffraction, fine increase of the X-ray reflectivity critical angle, displacement of the Ni $2p_{3/2}$ signal towards lower energy, significant increase of the electrical conductivity and decrease of the total transmittance. Quantification of Ni^{3+} by XPS method is discussed. We also showed that the use of Raman spectroscopy was relevant for demonstrating the presence of Ni^{3+} in the $Ni_{1-x}O$ thin films.

1. Introduction

Nickel oxide (NiO) thin films have a wide range of applications due to their excellent chemical stability, optical and electrical properties, and other kind of properties and performances. They have been widely used and mostly studied as anodic coloration materials in inorganic smart windows and electrochromic devices [1–5]. They have been also studied as hydrogen and other gas sensor materials [6], thin film transistors [7] and capacitors [8]. As a promising candidate of p-type transparent conducting films [9], nickel oxide thin films have been investigated as hole-transport interlayers in optoelectronic devices [10] and thin film diodes [11]. Among many potential applications, nickel oxide thin films have been shown excellent properties and performances as anodic coloration materials in electrochromic devices and as *p*-type transparent semi-conductive materials in relevant devices.

There are several methods to prepare nickel oxide films. Among them, reactive magnetron sputtering methods including Direct Current (DC), Radio Frequency (RF), and High Power Impulse Mag netron Sputtering (HiPIMS) are the most popularly used methods [1,7,12,13]. Other methods such as chemical vapor deposition [3], electrodeposition [4], pulsed laser deposition [5], epitaxial [8], low-temperature combustion synthesis [10], sol-gel deposition [14], spray pyrolysis [15] and thermal evaporation [16] are also frequently used to prepared nickel oxide thin films according to different circumstances. All of the characterized and intensively studied properties of the nickel oxide thin films as the deposition conditions like the oxygen partial pressure showed various oxygen to nickel concentration ($Ni_{1-x}O$) and multiple nickel valences.

The oxidation state of the nickel in the NiO thin films is the key factor which impacts the physical properties such as the electrical conductivity and the optical transmittance Doping or substituting elements for nickel to improve the oxide films properties has also been investigated [17].

In this work, we have been interested in non-stoichiometric nickel oxide ($Ni_{1-x}O$) thin films with two potential applications motivation: anodic coloration layers in electrochromic devices [18,19] and p-type transparent conductive films [9]. In both of the

* Corresponding author.
E-mail address: barnabe@chimie.ups-tlse.fr (A. Barnabé).

http://dx.doi.org/10.1016/j.apsusc.2017.05.095

Table 1
$Ni_{1-x}O$ thin film deposition oxygen pressure conditions and their respective thickness, deposition rate and crystalline phases determined by XRD.

Sample No.	p_{O2} (Pa)	Thickness (nm)	Deposition rate (nm/min)	Crystalline Phases (in weight%)
#01.	0.00	250	8.2	Ni + NiO (ε)
#02	0.02	260	8.5	Ni + NiO (ε)
#03	0.04	300	9.9	Ni + NiO (55%)
#04	0.05	300	16.1	Ni + NiO (86%)
#05	0.07	290	20.0	NiO
#06	0.09	300	20.7	NiO
#07	0.13	300	11.0	NiO
#08	0.14	300	11.0	NiO
#09	0.16	250	10.3	NiO
#10	0.40	250	10.0	NiO
#11	0.60	300	9.0	NiO
#12	0.80	300	5.8	NiO
#13	1.00	300	4.7	NiO

two applications oriented properties and performances, preparation methods and deposition conditions, microstructures of the films, electrical and optical properties are all critical influential factors and closely correlated to those performances. But up to now, even if there are large amount of publications on the nickel oxide thin films, there are still many unclear properties and some understanding disparities among specific experimental results. All the deposition adjustable parameters, as for instance the different substrate materials [20], are still worthwhile to be further individually studied to advance understanding of the basic physics and chemistry and to promote the applications of the nickel oxide thin film materials.

In this work, we use DC reactive magnetron sputtering to prepare nickel oxide thin films within large range of oxygen concentration in order to induce various nickel oxidation states in the films. We use detailed structural, microstructural and spectroscopic analysis as well as electrical and optical measurements to characterize the thin films in order to obtain clear information about their properties.

2. Experimental details

Many $Ni_{1-x}O$ thin films were deposited on the soda lime glass substrate at room temperature using DC reactive magnetron sputtering by introducing various Ar/O_2 mixture gas flow, which can be converted into different oxygen partial pressures p_{O2} ($p_{O2} = (flow_{O2}/(flow_{O2} + flow_{Ar}) \times p_{tot})$) whereas the total pressure of deposition p_{tot} was kept the same for all films deposition at about 2 Pa. 60 mm in diameter round plate nickel metal target of 99.99% purity was used and distance between the target and the substrate was kept at about 100 mm. By controlling the deposition time and rate, we prepared a series of thin films with roughly similar thickness of around 300 nm under different oxygen partial pressures. The preparation conditions of $Ni_{1-x}O$ thin films numbered from #01 to #13 are listed in Table 1.

Before the deposition of the $Ni_{1-x}O$ films, all the glass substrates were cleaned in acetone, ethanol and deionized water with ultrasonic wave cleaning machine successively for 20 mins and then dried with nitrogen gas. Using a turbo molecular pump combined with a rotary pump, the sputtering chamber background vacuum reaches less than 3×10^{-3} Pa for each sample before its deposition. The sputtering gases flow input is mixed with argon (99.99%) and oxygen (99.99%) and the flow rates were controlled with mass flow controllers separately. Metal nickel target was pre-sputtered in an argon atmosphere for 5 min to remove the contaminations on surface before each new deposition. The thickness of the deposited films was measured using a Dektak 3030ST mechanical profilometer along a step made through a shadow mask during the deposition. The crystal structural properties and the accurate thickness and density of the samples were analyzed by Grazing Incidence X-ray diffraction (GI-XRD) and X-Ray Reflectivity (XRR) using a Bruker-AXS D8-Advance X-ray diffractometer equipped with a copper source ($\lambda CuK_{\alpha 1} = 1.5405$ Å and $\lambda CuK_{\alpha 2} = 1.5445$ Å), a Göbel mirror and Bruker LynxEye detector used in 0D/1D mode. The GI-XRD data were analyzed with the Bruker-EVA software, JC-PDF database and refined with the Rietveld method implemented in the FullProf-Suite program. The XRR data were treated with the Bruker-LEPTOS software. The surface morphologies were analyzed by Atomic Force Microscopy (AFM) with a NanoScope III Dimension 3000 microscope. A Thermo Scientific K-Alpha apparatus was used for X-ray photoelectron spectroscopy (XPS) measurements, using a monochromatic Al Kα radiation (1486.6 eV) with a 400 μm spot size. Peaks were scanned at 50 eV pass energy. The spectrometer was equipped with ions gun which has been used to clean the surface of the sample (200 eV during 180 s). The binding energies (BE) have been referenced to the 1 s carbon peak (atmospheric contamination) at 284.9 eV. Raman spectra were collected by using a LabRAM HR 800 Jobin Yvon spectrometer with a laser operating at 532 nm. Spectra acquisition was carried out with a × 100 objective lens and 600 g mm^{-1} grating. The electrical conductivity at room temperature of the films was measured in four probes mode using the line configuration with a spacing between probes of 1.6 mm. The sizes of the film were used to calculate the shape factor correction (S) [21]. The optical transmittance and reflectance spectra were measured using a Bentham PVE300 sphere integrated UV–vis spectrophotometer over a wavelength range of 300–1100 nm at the room temperature.

3. Results and discussion

3.1. Deposition rate

As for the design of the experiment, the condition of the film deposition, like the deposition time, the power and the pressure of oxygen were fixed. The film thicknesses are systematically measured by profilometry and reported in Table 1. According to the fixed deposition time, the deposition rate has been calculated and also reported in Table 1 for each oxygen partial pressure (p_{O2}). The deposition rate is strongly dependent on p_{O2} and it can be divided into two parts. In the first part whereas $p_{O2} < 0.1$ Pa, i.e. for samples #01 to #06, the deposition rate grows up to the maximum rate of 20.7 nm/min with the gradually increasing oxygen partial pressure. This phenomena is well known in reactive sputtering process [22–24] and is due to the progressive incorporation of oxygen in the metallic growing layer when p_{O2} is increased. In the second part whereas $p_{O2} > 0.1$ Pa, i.e. for samples #07 to #13, we can observe that the deposition rate decreases dramatically in two steps when the oxygen partial pressure increases. It can be explained by the reaction of the oxygen with the target erosion zone which lead to the formation of less conductive oxide layer at the surface of the metallic nickel and a strong decrease of the target voltage associated to a decrease of the deposition rate.

3.2. Structural properties

The GI-XRD patterns of the films deposited at different oxygen partial pressures (samples #01 to #13) are presented in Fig. 1a.

The variation of the oxygen partial pressure induces big difference on the structure of the deposited films. For the lower p_{O2}, i.e. for samples #01 and #02, characteristic (111), (200) and (220) Bragg's peaks of Ni metal (space group F m–3 m with $a \approx 3.523$ Å) are clearly visible. With the increase of p_{O2}, the NiO face-centered cubic rock salt structure (space group F m–3 m with $a \approx 4.2$ Å)

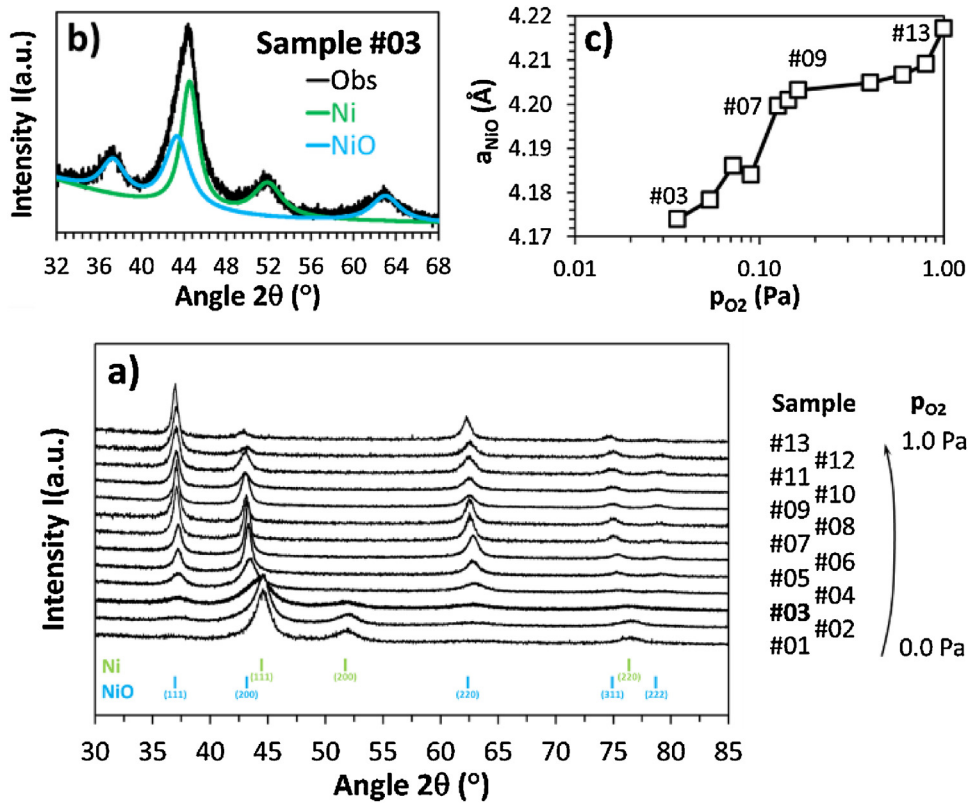


Fig. 1. a) GI-XRD patterns of samples #01 to #13 deposited at different oxygen partial pressure p_{O2}. b) Zoom of the GI-XRD pattern of sample #03 which exhibit the Ni and NiO phases mixture as determined by Rietveld refinement. c) $Ni_{1-x}O$ lattice parameter versus p_{O2} deduced from Rietveld refinement.

appears notably through the increase of the (111), (200), (220), (311) and (222) Bragg's peaks between 30° and 85° in the 2θ range. Even for the very low p_{O2} deposition conditions (sample #02 deposited at p_{O2} = 0.02 Pa but also for sample #01 deposited in pure Ar), very weak and broad peaks located at 2θ ≈ 37.3 and 63.0° are visible indicating that a few amount of nanocrystallized NiO could already be present in these samples. In these cases, the NiO phase is not really quantifiable due to the weaknesses of the peak and was noted as ε in Table 1. For sample #03 (Fig. 1b), both Ni and NiO phases are present and quantifiable in the 45%^{w} to 55%^{w} ratio respectively. Ni metal is still detectable for sample #04 at 14%^{w} but completely vanishes for samples #05 (p_{O2} = 0.07 Pa) and all the other films deposited at higher p_{O2}.

With the increase of the oxygen partial pressure during the deposition process, the lattice parameter of the $Ni_{1-x}O$ phase (a_{NiO}) continuously evolves as shown in Fig. 1c. A large change is first observed from sample #03 (a = 4.174(2) Å) to sample #07 (a = 4.1996(6) Å) and then followed by a smoother increasing up to sample #13 (a = 4.2172(1) Å). The first increase corresponds to the stabilization of the stoichiometric bunsenite NiO phase in low oxygen partial pressure. Ni^0 tends to be fully oxidized in Ni^{2+} as demonstrated by the disappearance of Ni metallic phase after p_{O2} ≈ 0.07 Pa (sample #05). Lattice parameter of sample #07 is close to the one of the bulk reference [25]. The second increase from sample #07 to sample #13, i.e for p_{O2} > 0.13 Pa, could be attributed to the increase of nickel vacancies and concomitant introduction of Ni^{3+} species (even if ionic radii of Ni^{3+} is smaller than the one of Ni^{2+} in 6-fold octahedral coordination) as previously reported by many authors [26,27]. This phenomenon expands for the highest p_{O2}. One can note that the peak of Ni_2O_3 is never observed as crystalline phase in this work.

No specific preferred orientation is observed for the NiO phase in sample #07, but a (111) preferred orientation tends to increase

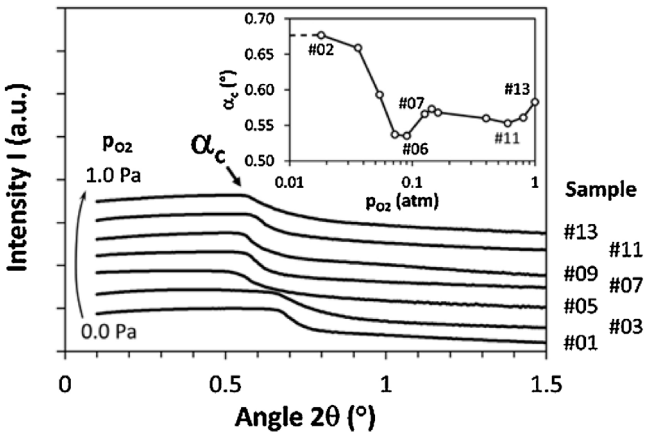


Fig. 2. XRR spectra of selected samples and evolution of the critical angle as a function of the oxygen partial pressure in inset.

from sample #07 to sample #13 (i.e. for p_{O2} > 0.13 Pa) as previously observed in similar films [28,29]. In the cubic NiO rock salt structure, the (111) plane corresponds to the pure compact plane of oxygen. With the oxygen partial pressure increasing, the {111} family plane shift away might be due to excess oxygen segregation at the grain boundaries [30]. Given by Seo et al. [26], this phenomenon is relevant with the increasing nickel vacancies because oxygen content is raised.

In addition to GI-XRD analysis, the surface-sensitive analysis of all the $Ni_{1-x}O$ films have been carried out by specular X-Ray Reflectivity (XRR) and presented in Fig. 2 for selected samples.

In the XRR spectra, thickness oscillations of X-ray intensity are not visible due to the high thickness of the samples. A simple model made of glass substrate (infinite thickness, ρ_{Glass} = 2.38 g cm^{-3} and

roughness <1 nm independently characterized) and NiO layer was implemented in the Bruker-Leptos program. For each deposited film, experimental XRR data were fitted with the genetic method and allow to refine the thickness, roughness and density (ρ) variables of the film. The critical angle (α_c) which is directly proportional to the electron density ($\alpha_c \propto \sqrt{\rho_{e^-}}$) and deduced from this refinement, is reported for all the samples in the inset of Fig. 2.

The critical angles obtained for films deposited under different oxygen partial pressures are very different. The dense nickel metal leads to the large critical angle under lower oxygen partial pressure. From sample #01 to #06, i.e. in the $0.0 \leq p_{O2} \leq 0.09$ Pa range, the critical angle rapidly decreases from $\alpha_c = 0.67^\circ$ down to 0.54°. With nickel reacting to the oxygen, the critical angle gets smaller due to the decrease of the density of the film ($\rho_{Ni} = 8.91\ g\,cm^{-3}$; $\rho_{NiO} = 6.72\ g\,cm^{-3}$). This behavior is also in good agreement with the increase of the deposition rate (Table 1) and the concomitant disappearance of the metallic Ni phase previously observed by GI-XRD (Fig. 1) in this p_{O2} range.

For $p_{O2} > 0.10$ Pa, i.e. for sample #09 up to sample #13, the critical angle is quite stable at around $\alpha_c \approx 0.56^\circ$. One can note a constant increase of the critical angle for the three samples deposited with the highest oxygen partial pressure. This could be correlated to the increasing of the nickel vacancies as the formation of one nickel vacancy is accompanied by transition of two Ni^{2+} ions to Ni^{3+} ions (if it supposed that all Ni^{3+} ions are resulted from the formation of Ni vacancies) [31]. However the true nature of the non-stoichiometry taking place in nickel oxide based thin films when p_{O2} increases, i.e. when an increase in Ni^{3+} concentration occurs, showing an increase in the critical angle still needs to be clarified.

For a better understanding of this behavior, NiO thin films deposited under various oxygen partial pressures were examined by X-ray Photoelectron Spectroscopy (XPS) and Raman spectroscopy. A commercial oxygen-rich "black" NiO powder was also analyzed for comparison. The corresponding XPS and Raman spectra are presented in Fig. 3.

Fig. 3a shows the XPS spectra of four specific films (not listed in Table 1) deposited in identical condition but with different oxygen partial pressures (0.04, 0.05, 0.11 and 0.16 Pa) in the p_{O2} range whereas the Ni^0 metal is oxidized into Ni^{2+} and potentially Ni^{3+} as previously determined by GI-XRD and XRR studies with the approximate threshold pressure of $p_{O2} \approx 0.1$ Pa.

Many published articles related to nickel oxides attempted to determine the Ni^0, Ni^{2+} and Ni^{3+} concentration by the assignation of oxidation states to single identifiable peak in the Ni $2p_{3/2}$ signal (Binding Energies BE ≈ 850–870 eV) obtained by X-ray Photoelectron Spectroscopy (XPS). For example Carley et al. [32] proposed assignment of BEs of 852.6, 854.6 and 856.1 eV to Ni $2p_{3/2}$ XPS spectra for Ni^0, Ni^{2+} and Ni^{3+} respectively. However more recent work from Biesinger et al. [33,34] shows that envelope spectra are better fitted by using multiplet splitting. Due to peak asymmetries, complex multiplet splitting, shake-up and plasmon loss structure, overlapping binding energies, it is quite difficult to determine the proportion of different Ni valences. Moreover the possible presence of residual surface contaminant like hydroxide or oxyhydroxide species after soft surface cleaning by etching can lead to additional misinterpretations on the presence of Ni^{3+} in the NiO phase. So we will conduct only a qualitative comparison.

On the one hand, no significant difference can be observed for all samples in the Ni 2p XPS spectra related to the presence of Ni^{2+}/Ni^{3+} species (BEs higher than 853 eV). This suppose that oxygen containing species localized at the surface should be present even for the lowest oxygen partial pressure deposited sample. This is also consistent with the O 1s XPS spectra (not shown here) whereas peak located at around 530 eV is visible and reflects a local electron density around O atoms.

On the other hand, the spectra of the two samples deposited at the lowest oxygen partial pressure ($p_{O2} < 0.1$ Pa) clearly show a peak around 852.5 eV which can be definitely attributed to the presence of Ni^0. Quite logically the peak intensity for Ni^0 is more pronounced in the case of the sample deposited at lower oxygen pressure. Even if they are limited in our case for the determination of the presence of Ni^{3+} species, XPS measurements confirm however the presence of nickel metal in the samples deposited at oxygen partial pressure lower than 0.1 Pa according to the X-ray experiments. It also pointed out that the sample deposited at the lowest p_{O2} contains NiO nanocrystallized phase not quantifiable by XRD.

The Raman spectra in the 100–700 wavenumber range shows the characteristic peaks of NiO phase [35,36]. First-order Transverse Optical (TO) and Longitudinal Optical (LO) phonons modes are located at 380 and 492 cm^{-1} respectively. However, black NiO which is oxygen-rich phase ($Ni_{1-x}O$), presents also an additional peak that can be attributed to the non-stoichiometry. This peak is often described in the bibliography as a shoulder located in the left of the LO peak [37]. In our case, this extra peak is clearly shown in the spectra of the black NiO at 460 cm^{-1}. Mironova-Ulmane et al. [38] explained the activation of the peak at 450 cm^{-1} by magnetostriction effect responsible for a slight rhombohedral distortion in NiO.

From this characterization complementary to GI-XRD, XRR and XPS, we can deduce that, even for samples deposited without oxygen, a small quantity of NiO is formed inside the metallic nickel matrix. The spectra shown in Fig. 3b are normalized for comparison but the values of the real intensities of the LO peaks are given in the inset of Fig. 3b. Below $p_{O2} = 0.04$ Pa, this oxide is probably nanocrystallized and then cannot be correctly observed in XRD patterns. From the variation of the intensity of the LO Raman peak, the quantity of NiO phase even for the lower oxygen deposition pressures doesn't seem to be negligible. The formation of NiO when no oxygen is used during the deposition may originate from the background gas before process gas introduction, the different micro-leaks compensated by pumping system, and from the argon gas bottle. Raman shift of LO peaks stays nearly constant in the 530–535 cm^{-1} range below 0.1 Pa due to the presence of stoichiometric NiO. For higher pressures and particularly above around $p_{O2} = 0.1$ Pa (sample #06-#07), Raman shift increases significantly and approaches the value of the "black" NiO due to $Ni_{1-x}O$ being more and more oxygen-rich when the oxygen deposition pressure increased. Above $p_{O2} = 0.14$ Pa, the evolution of Raman shift of LO peak still continues but becomes slower. Above $p_{O2} = 0.13$ Pa, the growth of the peak at 460 cm^{-1} confirms that an oxygen-rich phase is deposited. In conclusion, the films deposited around $p_{O2} = 0.1$ Pa are closed to the NiO stoichiometry. Below this partial pressure threshold, the amount of oxygen is too low to form a pure NiO phase and a mixture of Ni metal and stoichiometric NiO is obtained. Above this pressure threshold, an oxygen-rich phase $Ni_{1-x}O$ is precipitated due to the excess of oxygen in the gas mixture.

3.3. Surface morphology

The atomic force microscope (AFM) isoscale images of three representative films (samples #01, #07 and #13 deposited at $p_{O2} = 0.00$, 0.13 and 1.00 Pa respectively) using the tapping mode are shown in Fig. 4. The bright regions of the images reflect the strong fluctuation which means there are high peaks and deep valleys on surface [12,30]. The dark regions are opposite. At $p_{O2} = 0.00$ Pa, the nickel and argon ions hit with each other very strongly and easily lead to the formation of crystalline phase [39]. Hence, for sample #01, the grain size are around 60 nm in diameter and film surface is rough with Ra = 9.1 nm. When the oxygen partial pressure increases up to $p_{O2} = 0.13$ Pa, the roughness decreases as well as the grain size but in lesser proportion. At $p_{O2} = 1.00$ Pa,

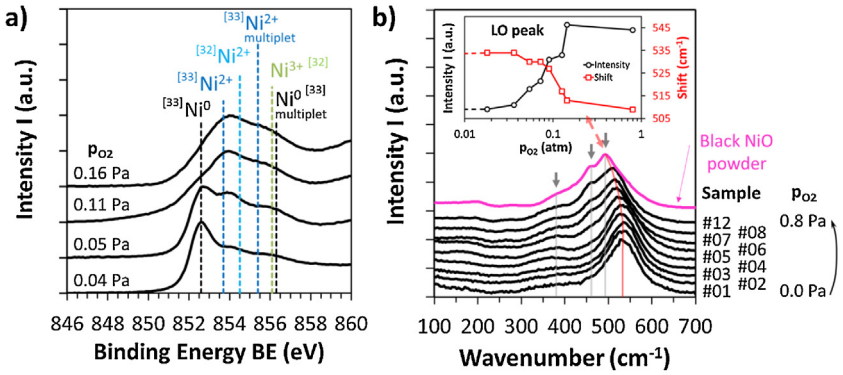


Fig. 3. XPS and Raman analysis spectra of the Ni-O thin films sputtered under different p_{O2} atmospheres: a) Ni 2p3/2 XPS spectra and comparison with bibliographical data from refs. [32] and [33]. b) Raman spectra in the 100–700 cm-1 range. LO Raman peak intensity and shift position are reported as function of p_{O2} in inset.

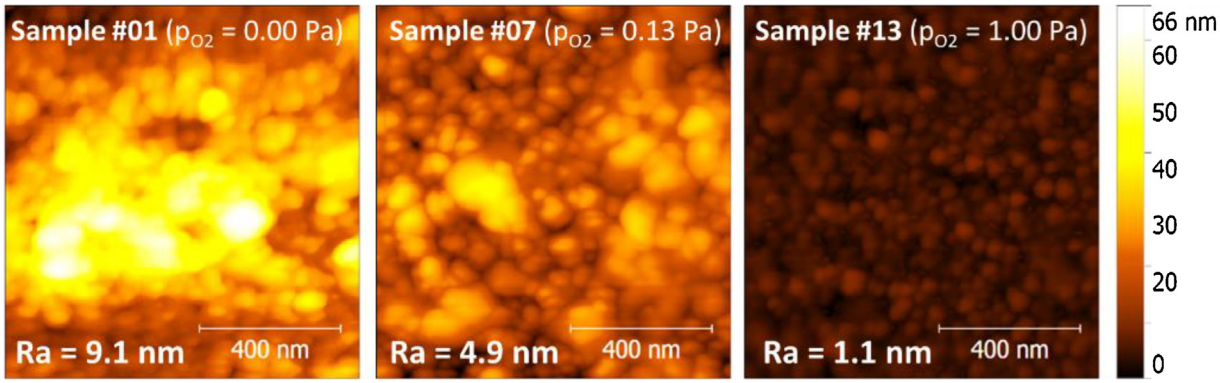


Fig. 4. AFM micrograph and roughness (Ra) of samples #01, #07 and #13.

Table 2
$Ni_{1-x}O$ thin film opto-electrical properties: electrical conductivity, average absorption coefficient in the 400–800 nm range and optical bandgap.

Sample No.	p_{O2} (Pa)	ρ (S/cm)	α (cm^{-1})	Eg (eV)
#01	0.00	2.16×10^{2}	2.32×10^{7}	1.81
#02	0.02	2.45×10^{2}	2.88×10^{7}	1.81
#03.	0.04	4.00×10^{1}	2.47×10^{7}	1.75
#04	0.05	3.10×10^{-4}	5.07×10^{6}	3.55
#07	0.13	3.01×10^{-6}	2.74×10^{5}	3.71
#08	0.14	6.15×10^{-6}	5.38×10^{5}	3.72
#11	0.60	2.78×10^{-5}	1.04×10^{6}	3.69
#12	0.80	5.70×10^{-5}	1.52×10^{6}	3.69

the film exhibits smoother surface. When the deposition process is conducted under an oxygen-enriched atmosphere, O• species are generated and accelerated to the substrate by promoting an increase of the bombardment of the growing layer and then, a smoothing of the surface. It may be also attributed to the increase of nickel vacancies. With the p_{O2} increasing, the Ni^0 species tend to disappear due to the combination of the nickel atoms with the free oxygen atoms. In conclusion, the variation of the oxygen partial pressure has a big influence on the surface morphology. Nevertheless, no significant influence of the oxygen pressure on the grains size has been noticed.

3.4. Electrical and optical properties

The electrical conductivities of the films were reported as the function of the p_{O2} in Table 2.

The most conducting films are those deposited under a low oxygen partial pressures ($p_{O2} < 0.05$ Pa): Sample #01 and sample #02 exhibit average electrical conductivities of 2.3×10^{2} S/cm. This high conductivity value could be explained by a current percolation trough a nickel clusters in the film [40]. The fact that this value is two order of magnitude smaller than the conventional attended value ($\sigma_{Ni} \approx 5 \times 10^{4}$ S/cm) of pure Ni (nanocrystalline bulk or film) [41,42] is consistent with the presence of oxidized Ni species highlighted previously.

When p_{O2} increases up to 0.14 Pa, the conductivity drastically decreases due to the increase of the NiO phase. The minimum conductivity value of 3.0×10^{-6} S/cm is reached at $p_{O2} = 0.13$ Pa for sample #07 because of the complete disappearance of the metallic nickel and the proximity of the perfect stoichiometric NiO composition which was highlighted by the previous analyses.

For higher p_{O2} values, the conductivity slightly re-increases up to 6×10^{-5} S/cm when the p_{O2} increases from the $p_{O2} = 0.13$ Pa to 0.80 Pa due to the appearance of nickel vacancies in the $Ni_{1-x}O$ material. These vacancies generate new charge carriers which contribute to the electrical conduction.

The total transmittance (TT) and reflectance (TR) as a function of the wavelength plotted for different oxygen partial pressures are reported in Fig. 5a and b. At each wavelength, the total absorbance (TA) has been calculated according to TT + TR + TA = 1 and reported in Fig. 5c. Knowing the thickness of each film, the absorption coefficient (α) has been calculated according to Eq. (1) for every wavelength. An average value of α in the visible range ($400 \leq \lambda \leq 800$ nm) is reported in Table 2.

$$\alpha = \frac{1}{t} \ln \left(\frac{(1 - TR)^2}{TT} \right) \quad (1)$$

Pictures of the films placed on a medium of patterned paper and values of their average total transmittance in the 400–800 nm

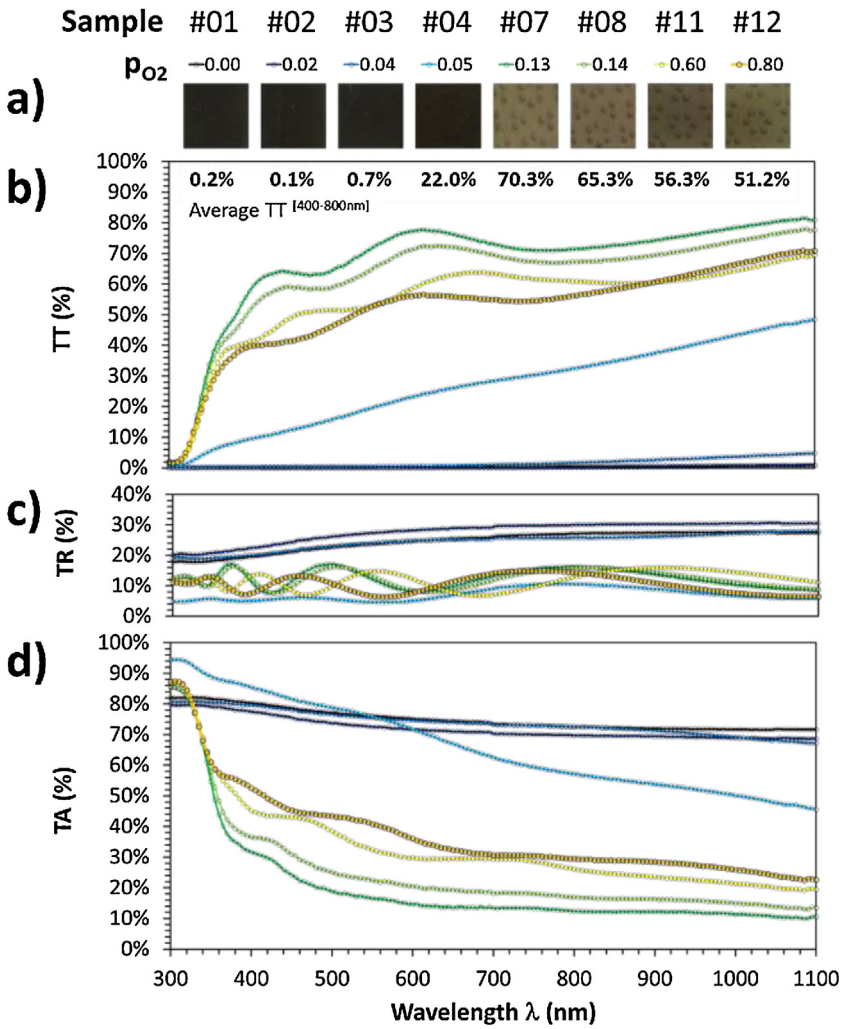


Fig. 5. Optical properties of NiO thin films sputtered under different p_{O2} atmosphere. a) Pictures of the films placed on a medium of patterned paper. b) Total Transmittance (TT) spectra. To illustrate the transparency of the films to natural white light, values of their average total transmittances in the 400–800 nm visible range are also indicated. c) Total Reflectance (TR) spectra. d) Total Absorbance (TA) spectra.

visible range are presented in Fig. 5a and b respectively to highlight that the optical properties drastically varies with the oxygen partial pressure.

For the thin films deposited at $p_{O2} < 0.05$ Pa and represented by the black and blue curves in Fig. 5: the total transmittance is very low and cannot be distinguished from the wavelength axis. The films are dark/colored and exhibit the highest reflectance of the whole series. This behavior is explained by the proportion of nickel metal (cluster) in the film which still important with these oxygen pressures.

The maximum transmittance in the visible range is obtained for sample #07, i.e. for $p_{O2} = 0.13$ Pa which corresponds to the mainly NiO stoichiometric composition. More than 70% of average total transmittance in the visible range is obtained. The minimum of the absorption coefficient α established on the whole wavelength range has been also obtained for this film.

For the film deposited at $p_{O2} > 0.13$ Pa, the total reflectance of the films stays in the 10% range while the total transmittance slightly decreases. The inter-fringes present in the TT spectra are almost similar which is consistent with the lower thickness variation of the films with p_{O2}.

The optical gap reported in Table 2 have been determined by the direct band gap Tauc's relation $((\alpha h\nu) = A\ (h\nu - Eg)^{1/2})$ [43] employed from the integrated transmittance data. As shown in Table 2, the direct band gap energy Eg increases drastically from 1.8 eV to 3.8 eV when the oxygen partial pressure increases from $p_{O2} = 0$ to 0.13 Pa. Once again, the presence of a band gap even for $p_{O2} = 0.00$ Pa prove the presence of oxidized nickel (no band gap should be obtained for pure metallic nickel phase). The maximum Eg value is equal to the 3.8 eV for $p_{O2} = 0.13$ Pa. The direct band gap energy is almost constant for higher oxygen pressures. This value is in agreement with those obtained in the literature [44,15,45] for the NiO phase.

4. Conclusion

The $Ni_{1-x}O$ films show apparent dependence on the variation of oxygen partial pressure p_{O2} during the deposition process. In addition with the deposition rate analysis, a complete set of structural, microstructural and opto-electrical characterizations proves that the deposition condition used in this work allows to obtain various nickel oxidation states (Ni^0, Ni^{2+}, Ni^{3+}) in the whole series.

When the $0.00 \leq p_{O2} \leq 0.05$ Pa, metallic nickel phase is detected by the GI-XRD, XRR and XPS technics. At the same time, GI-XRD, XRR, XPS and Raman spectrum analysis reveal that NiO is always present in these samples as minor phase. In these samples, opto-electrical properties are driven by the metallic phase (high total optical reflectance and high electrical conductivity values) but

affected in a measurable way by the small quantity of NiO formed inside the metallic Ni matrix.

Metallic nickel completely vanishes for $p_{O2} > 0.05$ Pa.

For higher p_{O2}, i.e. $p_{O2} > 0.10$ Pa, the evolution of lattice parameter determined by Rietveld refinement as well as the preferred crystallographic orientation, XRR-critical angle, Ni 2p3/2 XPS spectra, Raman Longitudinal Optical (LO) phonon modes, electrical conductivity, absorption coefficient, direct optical bandgap and surface topology (AFM) tends to prove that the stoichiometric NiO is obtained for $p_{O2} \approx 0.10$ Pa. Nickel vacancies and concomitant introduction of Ni^{3+} species gradually appears for $p_{O2} > 0.10$ Pa without sign of additional Ni_2O_3 phase in the films. Therefore, the as-deposited films obtained in this work can be represent as Ni + ε NiO ($0 \leq p_{O2} \leq 0.05$ Pa), NiO ($pO_2 \approx 0.10$ Pa) and $Ni_{1-x}O$ ($0.13 \leq p_{O2} \leq 1.00$ Pa).

Acknowledgments

This work was supported by the National Program on Key Research Project (2016YFB0303901) and the Beijing Natural Science Foundation (2161001).

The authors gratefully acknowledge the support of the Fédération de Recherche FERMAT (Fluides, Energie, Réacteurs, Matériaux et Transferts) in Toulouse for X-ray reflectometry measurements.

References

[1] R.T. Wen, C.G. Granqvist, G.A. Niklasson, Anodic electrochromism for energy-efficient windows: cation/anion-based surface processes and effects of crystal facets in nickel oxide thin films, Adv. Funct. Mater. 25 (22) (2015) 3359–3370.
[2] I. Bouessay, A. Rougier, P. Poizot, J. Moscovici, A. Michalowicz, J.M. Tarascon, Electrochromic degradation in nickel oxide thin film: a self-discharge and dissolution phenomenon, Electrochim. Acta 50 (18) (2005) 3737–3745.
[3] T. Maruyama, S. Arai, The electrochromic properties of nickel oxide thin films prepared by chemical vapor deposition, Sol. Energy Mater. Sol. Cells 30 (3) (1993) 257–262.
[4] A.C. Sonavane, A.I. Inamdar, P.S. Shinde, H.P. Deshmukh, R.S. Patil, P.S. Patil, Efficient electrochromic nickel oxide thin films by electrodeposition, J. Alloys Compd. 489 (2) (2010) 667–673.
[5] I. Bouessay, A. Rougier, B. Beaudoin, J.B. Leriche, Pulsed laser-deposited nickel oxide thin films as electrochromic anodic materials, Appl. Surf. Sci. 186 (1–4) (2002) 490–495.
[6] P.C. Chou, H.I. Chen, I.P. Liu, C.C. Chen, J.K. Liou, K.S. Hsu, W.C. Liu, Hydrogen sensing performance of a nickel oxide (NiO) thin film-based device, Int. J. Hydrogen Energy 40 (1) (2015) 729–734.
[7] D.J. Yun, S.W. Rhee, Deposition of NiOx thin films with radio frequency magnetron sputtering and their characteristics as a source/drain electrode for the pentacene thin film transistor, J. Vac. Sci. Technol. B 26 (5) (2008) 1787–1793.
[8] K.C. Liu, M.A. Anderson, Porous nickel oxide/nickel films for electrochemical capacitors, J. Electrochem. Soc. 143 (1) (1996) 124–130.
[9] P. Zhai, Q. Yi, J. Jian, H. Wang, P. Song, C. Dong, X. Lu, Y. Sun, J. Zhao, X. Dai, Y. Lou, H. Yang, G. Zou, Transparent p-type epitaxial thin films of nickel oxide, Chem. Commun. 50 (2014) 1854–1856.
[10] S. Bai, M. Cao, Y. Jin, X. Dai, X. Liang, Z. Ye, M. Li, J. Cheng, X. Xiao, Z. Wu, Z. Xia, B. Sun, E. Wang, Y. Mo, F. Gao, F. Zhang, Low-temperature combustion-synthesized nickel oxide thin films as hole-transport interlayers for solution-processed optoelectronic devices, Adv. Energy Mater. 4 (2014) 1301460.
[11] W.Y. Lee, D. Mauri, C. Hwang, High-current-density ITOx/NiOx thin-film diodes, Appl. Phys. Lett. 72 (13) (1998) 1584.
[12] H.L. Chen, Y.S. Yang, Effect of crystallographic orientations on electrical properties of sputter-deposited nickel oxide thin films, Thin Solid Films 516 (16) (2008) 5590–5596.
[13] D.T. Nguyen, A. Ferrec, J. Keraudy, M. Richard-Plouet, A. Goullet, L. Cattin, L. Brohan, P.Y. Jouan, Ellipsometric and XPS characterization of transparent nickel oxide thin films deposited by reactive HiPIMS, Surf. Coat. Technol. 250 (2014) 21–25.
[14] A.E. Jiménez-González, J.G. Cambray, Deposition of NiOx thin films by sol–gel technique, Engineering 16 (1) (2000) 73–76.
[15] P.S. Patil, L.D. Kadam, Preparation and characterization of spray pyrolyzed nickel oxide (NiO) thin films, Appl. Surf. Sci. 199 (1–4) (2002) 211–221.
[16] I. Porqueras, E. Bertran, Electrochromic behaviour of nickel oxide thin films deposited by thermal evaporation, Thin Solid Films 398–399 (2001) 41–44.
[17] G.B. Cho, T.H. Kwon, T.H. Nam, S.C. Huh, B.K. Choi, H.M. Jeong, J.P. Noh, Structural and electrochemical properties of lithium nickel oxide thin films, J. Chem. 2014 (2014), ID 824083.
[18] D. Dong, W. Wang, G. Dong, Y. Zhou, Z. Wu, M. Wang, F. Liu, X. Diao, Electrochromic properties of NiOx:H films deposited by DC magnetron sputtering for ITO/NiOx:H/ZrO2/WO3/ITO device, Appl. Surf. Sci. 357 (2015) 799–805.
[19] X. Song, G. Dong, F. Gao, Y. Xiao, Q. Liu, X. Diao, Properties of NiOx and its influence upon all-thin-film ITO/NiOx/LiTaO3/WO3/ITO electrochromic devices prepared by magnetron sputtering, Vacuum 111 (2015) 48–54.
[20] K.N. Manjunatha, S. Paul, Investigation of optical properties of nickel oxide thin films deposited on different substrates, Appl. Surf. Sci. 352 (2015) 10–15.
[21] F.M. Smits, Measurement of sheet resistivities with the four probes, Bell Syst. Tech. J. 37 (3) (1958) 711–718.
[22] Y.O. Jin, D. John, N.J. Podraza, T.N. Jackson, M.W. Horn, High temperature coefficient of resistance molybdenum oxide and nickel oxide thin films for microbolometer applications, Opt. Eng. 54 (2015) 037101.
[23] J. Hsu, C. Lee, Single- and dual-ion-beam sputter deposition of titanium oxide films, Appl. Opt. 37 (1998) 1171–1176.
[24] T.I. Selinder, E. Coronel, E. Wallin, U. Helmersson, α-alumina coatings on WC/Co substrates by physical vapor deposition, Int. J. Refract. Metals Hard Mater. 2 (2009) 507–512.
[25] Y. Kokubun, Y. Amano, Y. Meguro, S. Nakagomi, NiO films grown epitaxially on MgO substrates by sol–gel method, Thin Solid Films 601 (2016) 76–79.
[26] S. Seo, M.J. Lee, D.H. Seo, E.J. Jeoung, D.S. Suh, Y.S. Joung, I.K. Yoo, I.R. Hwang, S.H. Kim, I.S. Byun, J.S. Kim, J.S. Choi, B.H. Park, Reproducible resistance switching in polycrystalline NiO films, Appl. Phys. Lett. 85 (23) (2004) 5655–5657.
[27] H. Lipson, Elements of X-ray diffraction, Contemp. Phys. 20 (1) (1979) 87–88.
[28] H.L. Chen, Y.M. Lu, J.Y. Wu, W.S. Hwang, Effects of substrate temperature and oxygen pressure on crystallographic orientations of sputtered nickel oxide films, Materi. Trans. 46 (2005) 2530–2535.
[29] H.W. Ryu, G.P. Cho, W.S. Lee, J.S. Park, Preferred orientations of NiO thin films prepared by RF magnetron sputtering, J. Mater. Sci. 39 (2004) 4375–4377.
[30] Y.A.K. Reddy, A.S. Reddy, P.S. Reddy, Effect of oxygen partial pressure on the properties of NiO–Ag composite films grown by DC reactive magnetron sputtering, J. Alloys Compd. 583 (2014) 396–403.
[31] T.F. Chen, A.J. Wang, B.Y. Shang, Z.L. Lu, Y.L. Li, Y.S. Wang, Property modulation of NiO films grown by radio frequency magnetron sputtering, J. Alloys Compd. 643 (2015) 167–173.
[32] A.F. Carley, S.D. Jackson, J.N. O'Shea, M.W. Roberts, The formation and characterisation of Ni3+ –an X-ray photoelectron spectroscopic investigation of potassium-doped Ni(110)-O, Surf. Sci. 440 (1999) L868–L874.
[33] M.C. Biesinger, B.P. Payne, L.W.M. Lau, A. Gerson, R.St.C. Smart, X-ray photoelectron spectroscopic chemical state quantification of mixed nickel metal, oxide and hydroxide systems, Surf. Interface Anal. 41 (2009) 324–332.
[34] M.C. Biesinger, B.P. Payne, A.P. Grosvenor, L.W.M. Lau, A.R. Gerson, R.St.C. Smart, Resolving surface chemical states in XPS analysis of first row transition metals, oxides and hydroxides: Cr, Mn, Fe, Co and Ni, Appl. Surf. Sci. 257 (2011) 2717–2730.
[35] R.E. Dietz, G.I. Parisot, A.E. Meixner, Infrared absorption and raman scattering by two-magnon processes in NiO, Phys. Rev. B 4 (1971) 2302–2310.
[36] J.C. Lai, X.C. Wang, W.B. Mi, Y.H. Ding, B.H. Yang, Structure and optical properties of polycrystalline NiO films and its resistive switching behavior in Au/NiO/Pt structures, Phys. Rev. B 478 (2015) 89–94.
[37] S.H. Lee, H.M. Cheong, N.G. Park, C.E. Tracy, A. Mascarenhas, D.K. Benson, S.K. Deb, Raman spectroscopic studies of Ni–W oxide thin films, Solid State Ionics 140 (2001) 135–139.
[38] N. Mironova-Ulmane, A. Kuzmin, I. Steins, J. Grabis, I. Sildos, M. Pars, Raman scattering in nanosized nickel oxide NiO, J. Phys.: Conf. Ser. 93 (2007) #012039.
[39] I. Hotovy, J. Huran, L. Spiess, Characterization of sputtered NiO films using XRD and AFM, J. Mater. Sci. 39 (7) (2004) 2609–2612.
[40] U.P. Muecke, S. Graf, U. Rhyner, L.J. Gauckler, Microstructure and electrical conductivity of nanocrystalline nickel- and nickel oxide/gadolinia-doped ceria thin films, Acta Mater. 56 (2008) 677–687.
[41] M.J. Aus, B. Szpunar, U. Erb, A.M. El-Sherik, G. Palumbo, K.T. Aust, Electrical resistivity of bulk nanocrystalline nickel, J. Appl. Phys. 75 (1994) 7, http://dx.doi.org/10.1063/1.356076.
[42] R.A. Sayer, J. Zeng, H.H. Hsu, D. Peroulis, T.S. Fisher, Thermal and electrical conductivities of nanocrystalline nickel microbridges, J. Microelectromech. Syst. 21 (4) (2012) 850–858.
[43] J. Tauc, Optical properties and electronic structure of amorphous Ge and Si, Mater. Res. Bull. 3 (1968) 37–46.
[44] S. Hüfner, P. Steiner, I. Sander, F. Reinert, H. Schmitt, The optical gap of NiO, Zeitschrift für Physik B Condens. Matter 86 (2) (1992) 207–215.
[45] S. Hüfner, Electronic structure of NiO and related 3d-transition-metal compounds, Adv. Phys. 43 (2) (1994) 183–356.